

Synthesis of Lead Chalcogenide Nanocrystals by Sequential Ion Implantation in Silica

R. Espiau de Lamaestre,^{†,‡} J. Majimel,[§] F. Jomard,^{||} and H. Bernas^{*,†}

CSNSM/CNRS, Université Paris Sud, 91405 Orsay Campus, France, Fontainebleau Research Center, Corning SAS, 77210 Avon, France, CECM/CNRS, 94407 Vitry-sur-Seine, France, and LPSC/CNRS, 92195 Meudon Cedex, France

Received: May 23, 2005; In Final Form: July 18, 2005

Lead chalcogenide (PbS, PbSe, and PbTe) nanocrystals were synthesized by sequential implantation of Pb and one of the chalcogen species into pure silica. The implantation energy and fluence were chosen so that the implantation profiles practically overlap at a depth ≈ 150 nm with a maximum concentration of about 0.3 atom %. Annealing for 1–8 h at 850–900 °C triggers nanocrystal growth, which is monitored by high-resolution (HRTEM) and conventional transmission electron microscopy (TEM), secondary-ion mass spectrometry (SIMS), and Rutherford backscattering spectrometry (RBS). Striking differences are found in the depth distributions and microstructures of the resulting nanocrystals. We show that the differing chemical interactions of Pb and chalcogens (between each other and with silica) play a crucial role in chalcogenide nucleation and growth. Using available information on chalcogen redox states in silicate glass, we propose a nonclassical nucleation and growth mechanism consistent with our experimental results. The complex chemistry involved at the microscopic level is shown to impair control over the nanocrystal size distribution. Finally, PbS nanocrystal-doped silica is shown to emit intense photoluminescence (PL) in the 1.5–2 μm wavelength range, an effect that we relate to the above nucleation and growth scheme.

1. Introduction

Lead chalcogenide nanocrystals have been synthesized in glasses by various routes. The earliest one consists of introducing the components directly into the glass melt. After pouring and cooling of the glass, subsequent heating promotes a more or less controlled growth of nanocrystals. The method has been successfully applied to chalcogenide nanocrystal synthesis in various types of glasses: PbS (silicate glass),¹ PbSe (phosphate glass),^{2,3} and PbTe (borosilicate⁴ and silicate⁵ glasses). Synthesis control can usually only be achieved in rather limited composition and temperature ranges.

An apparently efficient way to overcome compositional limitations is to use the ion implantation technique to force solubility in any desired matrix. The use of ion beams with controlled energy and fluence obviously provides control over the initial dopants' depth distribution and concentration. Does it also lead to control over nanocrystal sizes and spatial distributions after the required postimplant annealing? Only PbS nanocrystal synthesis had been reported so far, via sequential implantation of Pb and S at high fluences ($2.5\text{--}7.5 \times 10^{16}$ $\text{at}\cdot\text{cm}^{-2}$) into pure silica, followed by annealing at 1000 °C.^{6–9} However, the size distribution was often found to be bimodal and uncontrolled. It is improved when going to low doses,⁷ but size distributions remain rather broad and close to a log-normal shape. We have shown¹⁰ that such lack of control must be related to the chemical interaction of sulfur with pure silica, which strongly influences S diffusion properties¹¹ as well as the

composition and structure of growing nanocrystals.¹² Here, we extend our previous studies of PbS formation to other ion implantation and annealing conditions and study PbSe and PbTe nanocrystal formation conditions as well. We show that the growth characteristics (crystalline structure, precipitation depth) of lead chalcogenide nanocrystals grown by annealing of sequentially implanted pure silica may be interpreted in terms of differences in the chalcogen chemical properties. We offer answers to the following questions: What is the chemical nature of the chalcogenide nanocrystals formed in this way? What is their nucleation mechanism? What is the influence of the chalcogen chemical state(s) on growth, and especially on size and depth control?

2. Chemistry of Chalcogens and Chalcogenides in Glasses

The chalcogen formal redox states generally range from $-II$ to $+VI$, depending on the concentration and redox interaction with their host.¹³ Such effects dominate in implanted glasses despite the latter's initially nonequilibrium character, simply because nanocrystal formation requires annealing at sufficiently high temperatures. Although they are in the same column of the periodic table, chemical properties vary when switching from S to Se, and even more so from Se to Te. Under given redox conditions (glass composition, temperature, and composition of the annealing atmosphere), they will be present in differing states. In silicate glasses, S may be found in $-II$ to $+VI$ redox states, whereas Se and Te are in $-II$, 0, and $+IV$ states. Oxidized forms are usually very mobile and volatile (e.g., the glass transition temperatures of SeO_2 and TeO_2 are, respectively, 317 °C and 450 °C). Reduced $-II$ forms are usually encountered as polychalcogenides, thus hindering their potential diffusion, and Te very often occurs as metallic precipitates. Among the three chalcogens, S is the one that has been most studied¹⁴ for technological reasons.

* Corresponding author. E-mail: bernas@csnsm.in2p3.fr. Telephone: +33 16915 5222. Fax: +33 16915 5268.

[†] CSNSM/CNRS, Université Paris Sud.

[‡] Fontainebleau Research Center, Corning SAS.

[§] CECM/CNRS.

^{||} LPSC/CNRS.

TABLE 1: E Is the Implantation Energy, R_p the Projected Range, and fwhm the Full Width at Half-Maximum of the Implantation Profile, According to SRIM Simulations.^a

	S	Pb	Se	Te	Pb
E (keV)	100	480	210	300	480
fluence (10^{15} at·cm ⁻²)	2.2	1.4	1.5	1.35	1
R_p (nm)	136	144	141	140	144
fwhm (nm)	108	67	101	87	67
max concentration (atom %)	0.30	0.30	0.21	0.23	0.22
annealing time (h)	1				
annealing temperature (°C)	800–950				

^a Also listed are the maximum concentrations at depth R_p , assuming an atomic density 6.5×10^{22} at·cm⁻³ (i.e., 2.17 g·cm⁻³) for SiO₂.

The influence of these chemical properties on the chalcogen diffusion properties is quite drastic.¹¹ The behavior of implanted Se is somewhat similar to that of implanted S, with the overwhelming fraction being in the immobile reduced form, while a small oxidized fraction (concentration below 100 appm) is very mobile. However, the oxidized form of Se may actually be in the +IV redox state (SeO₂), whereas that of S is more likely in the +VI state (SO₃),¹³ and their diffusion coefficients differ by one to 2 orders of magnitude, that of oxidized selenium being lower than that of oxidized sulfur.¹¹ Implanted Te is mainly in the atomic state and precipitates as Te metal upon annealing.¹¹ Because of their chemical interaction, chalcogen motion in turn has a major effect on Pb motion. As first shown in ref 12 and 15, the chemical state of sulfur not only determines the chemical nature of the precipitated phase but also the depth distribution of the nanocrystals via the Pb–chalcogen correlated diffusion properties. This is detailed below. We consequently expect, and find, significant differences in nucleation and growth behavior depending on the chalcogens that combine with Pb.

3. Experimental Section

It was previously shown^{6–9} that PbS cluster nucleation and early growth occur during implantation above concentrations around 10^{21} at cm⁻³. We thus restrict our studies to lower concentrations so as to observe precipitation from the earliest stage and also to enhance experimental accuracy in depth and radius distribution determination.

Pure Corning silica was sequentially implanted with Pb and one of the chalcogens at concentrations well below the aforementioned threshold (Table 1). Implantations were performed with the IRMA facility¹⁶ at CSNSM. Using the standard SRIM code,¹⁷ energies (and fluences) were chosen so that the projected range (and concentration at maximum) of both lead and the chalcogen would coincide. Rutherford backscattering (RBS) experiments were performed in a number of cases, using the ARAMIS accelerator¹⁸ at CSNSM with 1.2 MeV He, to determine Pb profiles. Such measurements also allowed us to check the Pb implanted fluence, which was systematically 30–40% higher than expected from ion current measurements during implantation, presumably due to sample charging effects. After implantation, samples were annealed in a quartz tube furnace at temperatures ranging from 800 to 900 °C for 1 h, under dry N₂ atmosphere, in order to minimize compositional changes in the glass during the anneal. Secondary ion mass spectrometry (SIMS) was performed with a Cameca IMS 4F probe at LPSC using a Cs⁺ primary beam. Secondary ion signals were detected using an electron multiplier. The ³⁰Si signal was simultaneously recorded in order to determine the surface position and to correct for detector efficiency. Depth calibration was achieved by postanalysis crater depth measurements with a Tencor Stylus profilometer, assuming a constant sputtering rate. Transmission

electron microscopy (TEM) was performed on (1) the CSNSM Philips CM12 microscope operating at 120 keV in order to observe the nanocrystal phases, radii, and depth distribution according to a procedure described elsewhere,¹⁰ and (2) the CECM JEOL 2010 high-resolution electron microscope (HREM) equipped with a field emission gun operating at 200 kV for crystallographic structure identification. To compare the elemental depth distribution as deduced from SIMS with the element concentration in the nanocrystal distribution, we evaluated the latter by (i) determining the radius and depth of each nanocrystal in the TEM cross-sectional micrographs, (ii) in a given depth slice, summing the nanocrystal volumes (deduced from their radius), and (iii) dividing by the average TEM cross-section thickness and the number of molecules (in crystalline form) per unit volume ($19.1 \text{ PbS} \cdot \text{nm}^{-3}$, $17.2 \text{ PbSe} \cdot \text{nm}^{-3}$, $14.9 \text{ PbTe} \cdot \text{nm}^{-3}$, $12.6 \text{ PbSO}_4 \cdot \text{nm}^{-3}$, $29.6 \text{ Te} \cdot \text{nm}^{-3}$). On a TEM micrograph, only a surface density of nanocrystals (i.e., surface concentration projected on the image plane along the direction of the electron beam) is measured. The thickness e of the cross-section sample, unless specified otherwise, was taken to be $e = 100$ nm (50–150 nm is a reasonable range of observable TEM sample thicknesses). As seen below (Figures 7–10), an error on the cross-section thickness may affect the agreement between the absolute quantities of elements as determined via TEM or SIMS, but it has no effect on the profiles and the profile modifications. Note that, in the following experiments, we used both TEM and photoluminescence to study the effect of reversing the (lead vs chalcogen) implantation sequence and found no significant differences. In the photoluminescence (PL) experiments conducted on (S + Pb) sequentially implanted samples (Section 6), an Ar laser operated at 488 nm was used for excitation; the sample's PL was collected by an optical fiber and dispersed by a Jobin Yvon TRIAX 320 spectrograph. The signal was detected by a PbS detector and corrected for the entire system collection efficiency using a tungsten lamp.

4. Results

Our previously reported SIMS measurements¹⁵ revealed definite discrepancies with the as-implanted concentration profiles expected from SRIM simulations. The Pb implanted profile was 20% larger and shifted to greater depths; on the other hand, S and Se distributions were closer to the surface than expected. Annealing in the range 850–900 °C/1 h led to clustering in all sequentially implanted samples, as shown below, and the postanneal nanocrystal depth distribution extended well beyond the initial concentration profiles. The evidence for (and consequences of) annealing-induced species diffusion are the main topic of this paper.

4.1. Phase Identification. The microstructure of all observed nanocrystal types was investigated by HRTEM. Several tens of precipitates were studied in each type of sample. Our results on Pb + S implanted silica, published elsewhere,¹² revealed growth not only of PbS (S in –II redox state) but also of PbSO₄ (S in +VI redox state) nanocrystals. In this case, a large fraction of the nanocrystals was polycrystalline, sometimes containing both the PbS and PbSO₄ phases (see Figure 1).

A similar structural behavior might have been expected in the case of Pb + Se implanted silica in view of the similarities between Se and S diffusion in silica. However, all observed lattice fringes spacings and zone axis (Figure 2) fully agreed with the standard $Fm\bar{3}m$ ($a = b = c = 6.13 \text{ \AA}$) cubic form of PbSe. Neither PbSeO₃ nor PbSeO₄ nanocrystals were observed. Moreover, only single crystals were found. To our knowledge, this is the first report of PbSe nanocrystal synthesis by sequential implantation in pure silica.

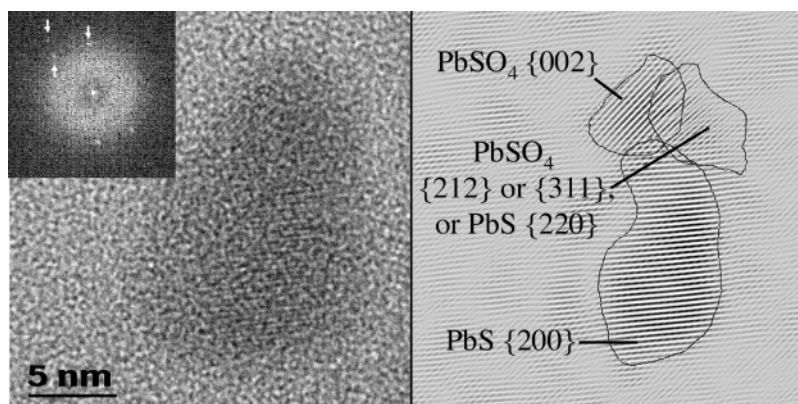


Figure 1. Example of polycrystalline PbS/PbSO₄ nanocrystal containing at least three domains differing by their interplanar distances and orientation. Inset: the FFT of the original image, showing three different couples of spots, indicating the presence of diffracting planes (arrow). In the FFT, one can filter the background so as to isolate the diffracting region corresponding to one particular couple of spots (filtered image on the left). See also ref 12.

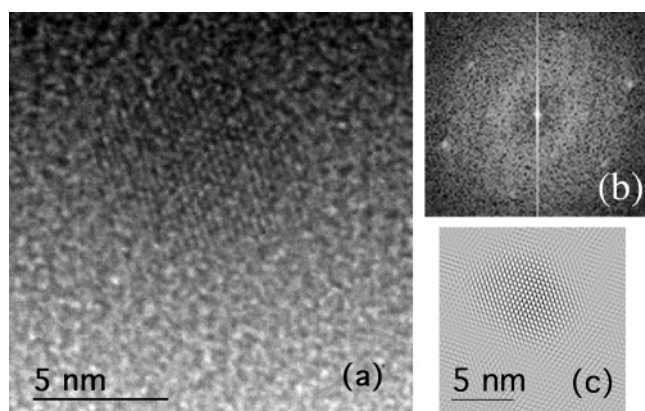


Figure 2. Zone axis [220] image of a cubic PbSe nanocrystal, showing two different interplanar distances $d_{200} = 3.06$ Å and $d_{111} = 3.54$ Å (a); FFT of the image, showing the symmetry of the zone axis (b); inverse FFT of the filtered FFT, so as to better isolate the nanocrystal lattice from the surrounding amorphous signal (c).

Structural identification in the case of Pb + Te sequentially implanted samples is not as straightforward. Almost all nanocrystals were monocrystalline (Figure 3), but phase identification by HRTEM was difficult because the interplanar distances of Te and PbTe are similar ($d_{010}^{\text{Te}} = 3.86$ Å close to $d_{111}^{\text{PbTe}} = 3.73$ Å; $d_{011}^{\text{Te}} = d_{200}^{\text{PbTe}} = 3.23$ Å; $d_{012}^{\text{Te}} = 2.35$ Å and $d_{110}^{\text{Te}} = 2.23$ Å close to $d_{220}^{\text{PbTe}} = 2.28$ Å). All our measured interplanar distances were compatible with both phases. From the zone axis symmetry, two of the nanocrystals were identified as Te, but the orientation of the majority did not allow discrimination between PbTe and Te.

4.2. Phase Evolution during Annealing. In the earlier growth stages (as soon as a PL signal is observed (see Section 6), for example, after a 30 min anneal at 850 °C) we found rather large clusters (diameter ≈ 6 nm) identified as crystalline PbS or PbSe, surrounded by very small clusters whose diameter was below 2 nm, all localized inside the implantation profile. None of these small clusters exhibited lattice fringes under HRTEM. They were presumably amorphous, and their chemical composition could not be determined. Photoluminescence (PL) experiments on the corresponding PbS samples detected no signal at wavelengths below 1 μm for any of our annealing conditions (see below, Section 6), whereas, had these small nanocrystals been crystalline PbS, we should have expected light emission in this region, according to the size–gap relation for PbS nanocrystals.¹⁹ Our TEM experiments revealed that these clusters progressively dissolved as growth proceeded, contribut-

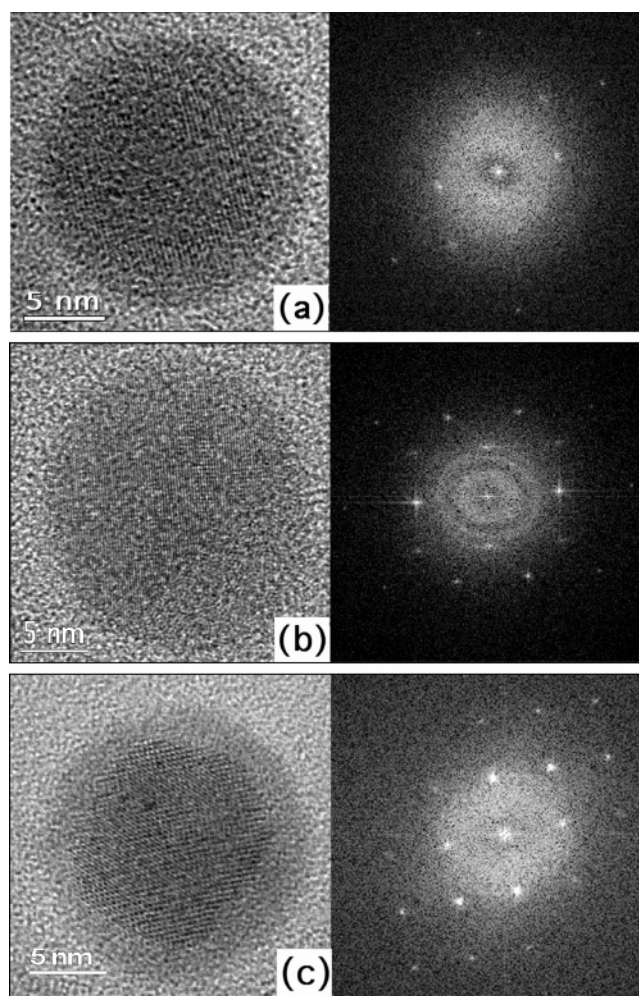


Figure 3. 3. PbTe [100] or Te zone axis (a) and (c). Te zone axis; the FFT of each image is on the right-hand side (b). In (c), the nanocrystal is probably melting under the electron beam.

ing to the growth of nearby PbS or PbSe nanocrystals (Figure 4a). Such nanocrystal growth, occurring via dissolution of preexisting amorphous clusters, is not at all typical of standard homogeneous nucleation. We suggest that it is due to the combination of chalcogen redox states in the case of PbS and PbSe (Figure 4b, see discussion in Section 5).

4.3. Postanneal Nanocrystal Depth Distribution: Influence of Chemistry. Sample annealing induced marked differences in the depth distributions of both the implanted constituents and

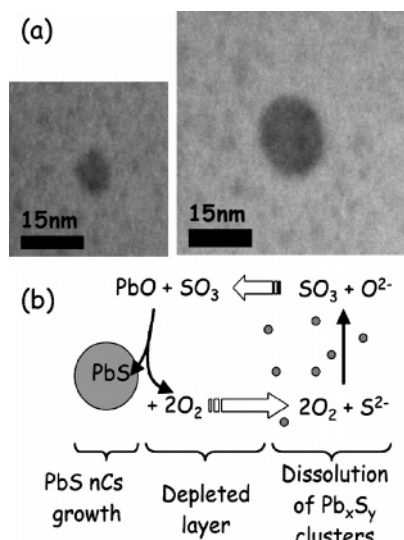


Figure 4. Pb + S sequentially implanted into silica after annealing at 850 °C/1 h. Examples of small amorphous precipitates in the depleted layer around large nanocrystals (a). Suggested mechanism of depleted layer formation (b).

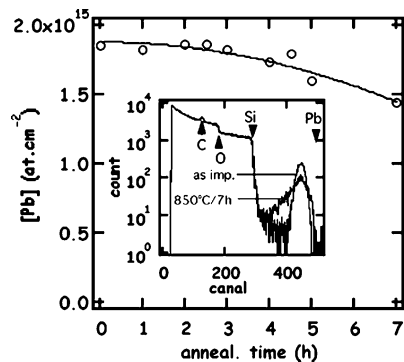


Figure 5. RBS measurement of Pb concentration ([Pb]) in S + Pb implanted sample with a 1.2-MeV He beam. Initial concentration was $1.88 \times 10^{15} \text{ Pb}\cdot\text{cm}^{-2}$ and decreased during annealing at 850 °C. Inset shows the RBS spectra for the as-implanted sample and after a 7 h anneal at 850 °C. Positions of the Pb, Si, O, and C surface peaks are indicated by an arrow (C was deposited before the RBS analysis so as to avoid sample charging during measurements).

the nanocrystals that they formed. RBS provided evidence (Figure 5) for very significant changes in the Pb concentration profile, even leading to a $\sim 20\%$ loss of Pb content from the samples after annealing up to temperatures corresponding to the nanocrystal formation range. These changes are a consequence of the differing chemical interaction of the chalcogens with SiO₂ or Pb. Figure 6 shows the nanocrystal density depth dependence as measured by TEM. Nanocrystal growth of all three chalcogenides clearly occurs well outside of the as-implanted profiles:^{11,15} on the far side of the profile for Pb + S implanted samples, on both sides of the implanted region for Se + Pb, and again chiefly on the far side of the Te + Pb implanted region. An understanding of these results requires a study of each chalcogen's chemical interaction with the host and with Pb.

4.3.1. Precipitation in the S + Pb Implanted Sample. As noted above, a detailed SIMS analysis¹⁵ showed that our Pb and S profiles were somewhat shifted in opposite directions as compared to those expected from SRIM simulations; this accounts for the shift in Figure 6a between the maximum concentration (arrow) and the maximum nanocrystal density, but certainly not for the nucleation and growth of PbS and

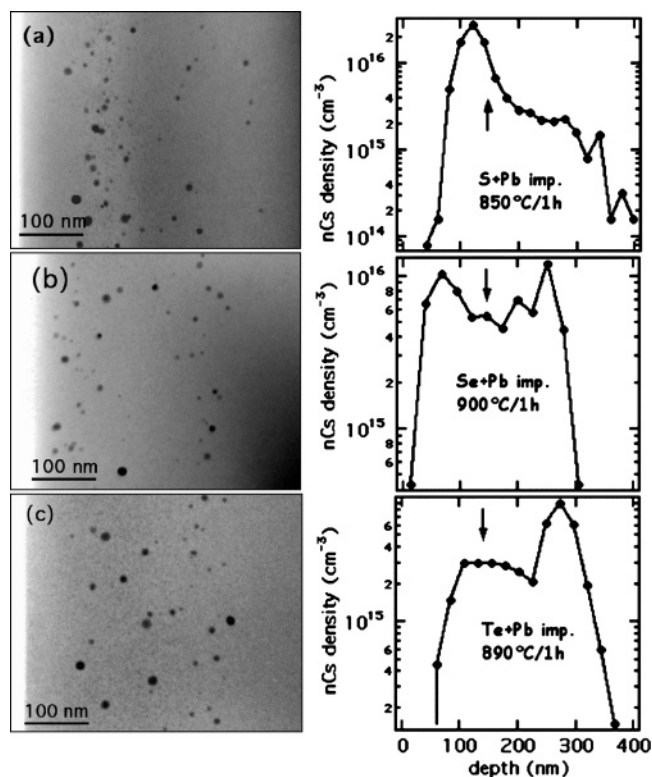


Figure 6. Left-hand side: Representative examples of TEM cross sections for different chalcogen implantation (SiO₂ surface is on left side of micrographs). S + Pb sequentially implanted silica; after annealing at 850 °C/1 h, nanocrystals grow on the low-depth side of the implanted profile (a). Se + Pb sequentially implanted silica; after annealing at 900 °C/1 h, nanocrystals grow on both outer sides of the implanted profile (b). Te + Pb sequentially implanted silica; after annealing at 900 °C/1 h, nanocrystals grow within and on the high-depth side of the implanted profile (c). Right-hand side: Measured density of nanocrystals in the same samples, determined by TEM. The arrow indicates the position of the initial Pb and chalcogen concentration maximum (Table 1): $R_p(\text{Pb}) = 144 \text{ nm}$; $R_p(\text{S}) = 136 \text{ nm}$; $R_p(\text{Se}) = 141 \text{ nm}$; $R_p(\text{Te}) = 140 \text{ nm}$.

PbSO₄ nanocrystals outside of the implanted profile. In refs 11 and 15, the Pb and S concentration profiles were determined independently after annealing of a sample implanted with only one of the elements. But in the sequentially implanted samples, the mobility of a species is affected both by its interaction with the other and by the occurrence of precipitation. Hence, we measured both the Pb and S concentration profiles in the *sequentially implanted* sample after annealing (Figure 7a), and checked that, as detailed in ref 15, the total amount of precipitated PbS (or PbSO₄) at a given depth is controlled by the least concentrated element. The fast-diffusing oxidized form of sulfur determines the depth distribution of PbS and/or PbSO₄ nanocrystals, leading to precipitation outside of the implanted profile.

We were unable to determine whether PbSO₄ is the main precipitated phase in the in-depth region ($z > 250 \text{ nm}$) of the sample. However, we observed both the PbS and PbSO₄ phases in a sample annealed 4 h at 900 °C, for which 70% of the nanocrystals had grown outside the implanted profile (Figure 7b). In most cases, we could not distinguish between the PbS and PbSO₄ structures; however, of the 12 precipitates whose structure was identified, five contained both the PbS and PbSO₄ phases and seven were PbSO₄. This suggests that equilibrium was reached between both sulfur redox states after sufficient annealing, facilitated by fast-diffusing SO₃ (see reaction 1, Section 5).

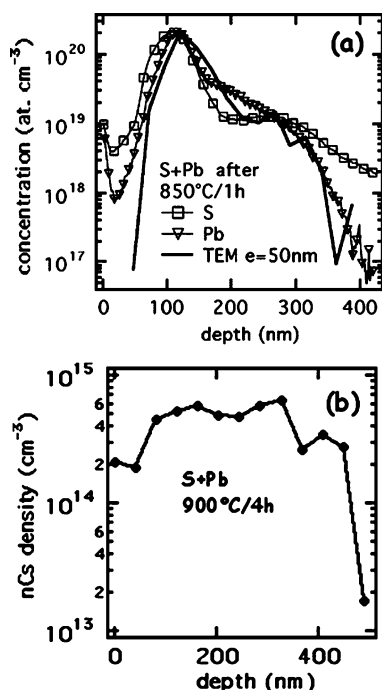


Figure 7. Total concentration profiles of Pb and S compared to the nanocrystal depth distribution measured by TEM (a). Sample thickness was taken as $e = 50$ nm so as to match SIMS concentration and TEM measurement. All samples were annealed 1 h at 850 °C. Precipitation is governed by the least-concentrated element. Nanocrystal density depth distribution in the same class of sample after annealing 4 h at 900 °C (b). More than 70% of the nanocrystals have grown outside of the initial ($70 < z < 200$ nm) implanted profile.

4.3.2. Comparison Between PbSe and PbS. Chalcogen diffusion experiments¹¹ showed that S and Se are chemically very similar as opposed to Te; when implanted into SiO₂, they both have two different oxidation states, one of which is quasi-immobile, whereas the other is very mobile. However, the oxidized form of selenium is likely the +IV state (versus +VI for sulfur), which is less mobile. In our Se + Pb sequentially implanted samples, the Se implantation energy and fluence were chosen so that the depth and concentration were identical to those of S in the S + Pb sequentially implanted samples of Table 1. But in this case, TEM experiments (Figure 6b) show that nanocrystals are preferentially synthesized on either side of (rather than inside) the implanted profile, in strong contrast to the (S + Pb) implanted sample, and SIMS profiling confirms that this is due to Pb and Se transport (Figure 8a). Moreover, the PbSe nanocrystals' average radii (Figure 8b) are larger on both sides of the implanted profile than in its center. Our results indicate that, although they are only a small fraction of the total, the mobile oxidized chalcogens play a major role in promoting nucleation and growth outside the implanted profile. Also, a comparison of the (S + Pb) and (Se + Pb) results clearly shows that the chemical interactions of chalcogens with both the host and the sequentially implanted Pb affect the depth at which nucleation and growth occur.

4.3.3. The Special Case of PbTe/Te. Nucleation and growth outside of the implanted profile was also observed after (Te + Pb) sequential implantation and annealing (Figure 6c). In Figure 9, we compare the initial concentration profile as determined by SRIM with the elements' concentration profile in precipitated form as measured by TEM. Because, as noted above, Te and PbTe precipitates could not be distinguished, the precipitated concentration was plotted, assuming 100% of one or the other. Approximately half of the precipitated concentration is outside

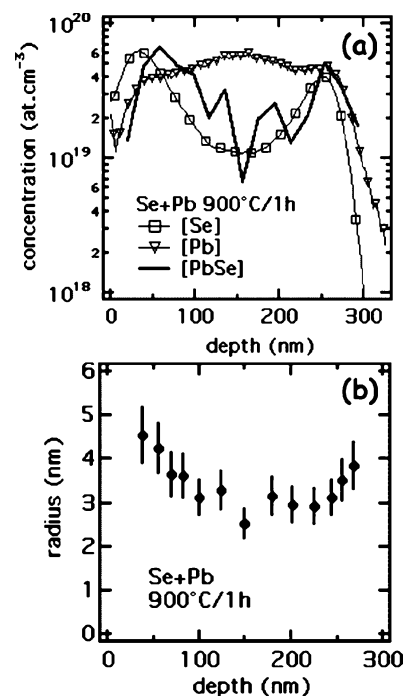


Figure 8. Growth characteristics of the sample annealed 1 h at 900 °C after Se + Pb sequential implantation in pure silica. Total concentration profiles of Pb (triangle) and Se (square) as measured by SIMS compared to those deduced from TEM via PbSe nanocrystals distribution (thick line) (a). The precipitated amount is governed by the least concentrated element. Depth dependence of PbSe nanocrystal radii (b). Each point is an average over 49 precipitates, its abscissa being the average depth and the ordinate their average radius. Error bars are statistical because of the finite averaging ensemble size.

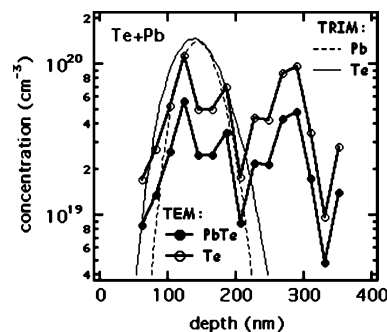


Figure 9. Comparison of initial concentration profiles of Pb and Te as determined by SRIM (Table 1) with the precipitated element concentration, as deduced from TEM under the assumption that all precipitates are either PbTe (full circles) or Te (empty circles). The sample is (Te + Pb) sequentially implanted silica annealed 1 h at 890 °C.

of the implanted profile. As we identified no very mobile form of Te in diffusion experiments, and because, contrary to the cases of S and Se,¹¹ no Te was found outside of the implantation profile when implanting the sample with Te alone and annealing under the same conditions, we cannot ascribe nucleation and growth outside of the implanted profile to diffusion. We suggest that the presence of Pb provides a chemical interaction that enhances Te mobility, leading to precipitation outside the implanted profile.

The Pb–chalcogen chemical interaction and its effect on the diffusion properties and precipitation can be evidenced by comparing the postanneal profile of the elements in SiO₂ when implanted alone or sequentially implanted. Figure 10a shows the effect on the sulfur concentration profile of identical anneals (1 h at 900 °C) for a S (or Pb) implanted sample versus a (S +

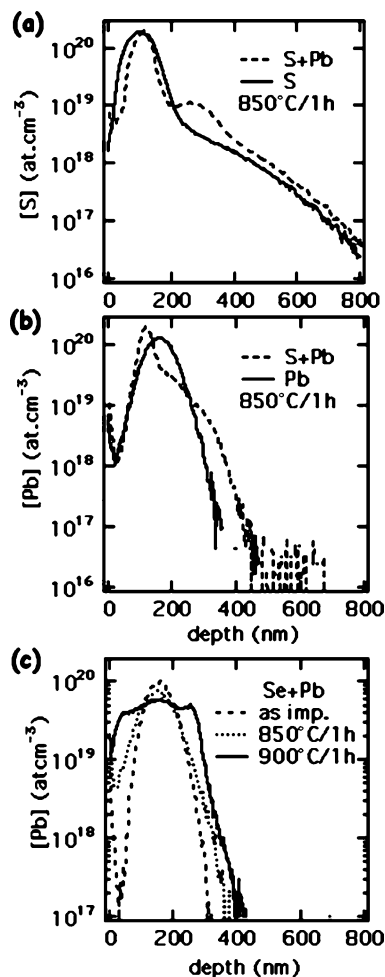


Figure 10. Modification of implanted atom mobility by the Pb-chalcogen interaction (from SIMS measurements). Comparison of S concentration after a 1 h anneal at 850 °C of S implanted and S + Pb implanted silica (a); comparison of Pb concentration after a 1 h anneal at 850 °C of Pb implanted and S + Pb implanted silica (b). Pb concentration in the Se + Pb sequentially implanted silica, after annealing at different temperatures (c). The difference between (b) and (c) illustrates the chalcogen's influence on Pb mobility.

Pb) implanted sample. In the latter case, while precipitation within the implanted profile leads to a decrease of the profile width, a well-known effect,²⁰ there is significant sulfur in-depth profile broadening due to precipitation with Pb. The latter element's profile is also broadened, its mobility being enhanced by its interaction with fast-moving sulfur (Figure 10b). In the case of the (Se + Pb) sample, a similar effect occurs (Figure 10c), except that nanocrystal formation now occurs on both slopes of the implanted profile rather on one side. The difference in chemical behavior of Se and S relative to Pb is presumably the source of this effect.

5. Discussion

5.1. Effect of Redox Properties on Nucleation. We have shown that chalcogenide nanocrystal formation in these sequentially implanted samples cannot be analyzed in simple nucleation theory terms. We discuss a possible mechanism for nanocrystal nucleation and growth that takes the known chemical properties into account and involves intermediate steps.

Upon annealing, slow-diffusing Pb combines with the reduced form of the chalcogen inside the implantation profile to form the small amorphous clusters identified in our (S + Pb) samples. The small, oxidized (e.g., SO₃ or SeO₂) chalcogen fraction is

likely a key factor of growth due to its much faster diffusion.¹¹ Growth of PbS and/or PbSO₄ then occurs by the two reactions:



The oxygen freed in these reactions diffuses inside the implanted profile, contributing to the dissolution of amorphous Pb polysulfide clusters, leading to PbO and to mobile SO₃ groups (e.g., via the reaction $\text{S}^{2-} + 2\text{O}_2 \rightarrow \text{SO}_3 + \text{O}^{2-}_{\text{glass}}$) so that, in turn, reactions 1 and 2 again promote PbS nanocrystal nucleation and growth. The process is summarized in Figure 4b. Nanocrystal synthesis may thus occur via different nucleation paths: (i) the reaction of free Pb with diffusing SO₃, leading to either PbSO₄ or directly to PbS, (ii) the reduction of PbSO₄ nanocrystals, (iii) the crystallization of small precursors Pb_xS_y (with the help of SO₃?), and possibly, (iv) the reaction of free lead with S²⁻. Analogous nucleation stages may be operative in the case of PbSe because of the chemical similarity between S and Se. For PbTe, whose chemistry differs markedly, nucleation mechanisms should also differ, but at least two distinct nucleation paths are possible: (i) direct formation of PbTe nanocrystals by the reaction of isolated Pb and Te or (ii) initial formation of Te nanocrystals (much less soluble in silica than Pb) and incorporation of Pb as annealing proceeds. Finally, and most importantly, the high diffusivity of the sulfate (or, to a lesser extent, sulfite) groups could explain why PbS nanocrystal growth tends to occur on the slopes of the implanted profiles (see below).

5.2. On Nucleation and Growth Outside of the Implanted Profile. According to classical nucleation and growth theory for an AB mixture,^{21,22} precipitation outside of the implanted profile should not occur. From the Gibbs–Thompson relation, the solubility of B at the surface of stable nanocrystals (with radius $R > R^*$) is lower than that of B at the surface of a nanocrystal with a critical radius R^* at the stability threshold. If precipitates have already reached the coarsening stage inside an implanted profile, the mean concentration of B in the A-rich phase is close to its solubility value at the average-size nanocrystal's surface. Were this picture valid in our systems, outdiffusion from the precipitate region should only lead to average concentrations below the stable nucleus formation limit. Nucleation and growth might then occur in precoarsening growth stages, but not once the majority of B has precipitated. This is in strong contrast to our observations. In the case of sequentially implanted (S + Pb) samples, for example, combined SIMS and TEM experiments show that essentially all the Pb and S are contained in a PbS + PbSO₄ nanocrystal profile after a 1 h anneal at 850 °C (Figure 7a), a profile that broadens continuously as annealing proceeds to higher temperatures and longer times (Figure 7b).¹⁰ Clearly, our sequentially implanted systems do not satisfy the criteria of classical theory.

In fact, of course, our samples are far from the binary mixture situation referred to above because three elements (the chalcogen, Pb and O) and their compounds are involved in growth. Kuehman and Voorhees²³ found that, in a ternary system in which coarsening involves three simultaneous Gibbs–Thompson relations, each of these depend on all diffusion coefficients and solubilities in the various constituent nanocrystal phases. Moreover, the compositional ratio varies greatly in our samples. For example, in the (S + Pb) sample annealed 1 h at 850 °C (Figure 7a), PbS and PbSO₄ nanocrystals are formed both in a Pb-excess region (at depths between 120 and 270 nm) and in a S-excess region (depths below 120 nm or beyond 270 nm). In

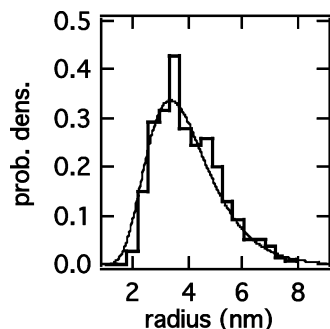


Figure 11. Example of size distribution in S + Pb implanted sample after annealing at 850 °C/1 h (400 precipitates). The thin line is the adjustment by a log-normal probability density function $f_{\log\text{-normal}}(R = r) = 1/(r \ln(\sigma)\sqrt{2\pi}) \exp(-(\ln(r/\mu))^2/2(\ln(\sigma))^2)$ with $\mu = 3.7$ nm and $\sigma = 1.4$.

the Se + Pb sample annealed at 900 °C/1 h (Figure 8), PbSe nanocrystals are formed both in a Pb-excess region (beyond 50 nm) and in a Se-excess region (below 50 nm); at the projected range of Se and Pb, the uncombined Pb concentration is at least 2–3 times larger than that contained in PbSe nanocrystals.

Redox chemistry, such as eqs 1 and 2, must be involved in the growth process, including the various redox states of the chalcogen and of all possible O states, such as 0 for O₂, or -II for O²⁻_{glass}, SeO₂, and PbO. A quantitative approach to the results should account not only for thermodynamical features (the equilibrium concentration of the oxidized forms, the chemical interaction between the oxidized and the reduced forms, the magnitude of the chemical interaction of each chalcogen with Pb), but also for the nucleation and growth kinetics (the diffusion of the oxidized form of Se being slower than that of S, the dissolution kinetics of small amorphous clusters formed inside the implantation profile, the dominating nucleation mechanism in the Se + Pb case...). This is clearly a very ambitious program for the future.

5.3. Nanocrystal Size Distributions. The present work was undertaken in an attempt to produce a high density of small nanocrystals for optical applications. Control over the average nanocrystal size and narrowness of the size distribution are thus a crucial feature. Our TEM pictures (Figure 6) show that, despite the differences described above in the diffusion coefficients and chemical state of chalcogens, the final average nanocrystal radii in our annealed samples were all quite similar ($\langle R \rangle_{\text{PbS}} = 2.8$ nm, $\langle R \rangle_{\text{PbSe}} = 3.45$ nm, $\langle R \rangle_{\text{PbTe or Te}} = 4.05$ nm), as were the size distributions. The latter are asymmetric, as shown in Figure 11, and approach a log-normal shape whose geometrical standard deviation is systematically about 1.45. A discussion of these features, on the basis of work²⁴ performed in various areas of growth science, is given in ref 10, which shows that their very existence testifies to the absence of any precise information on the growth process. Multiple nucleation and growth processes occur, as listed in the preceding paragraphs; their interference blurs the effect that each alone would have on the size distribution. This memory loss translates to a fast relaxation of the size distribution to its asymptotic log-normal shape. This interpretation is supported by the fact that, in the annealed (S + Pb) and (Se + Pb) samples, identical log-normal size distributions were found at different depths, i.e., whether the nanocrystals had grown inside or (after diffusing) outside of the initial implantation profile.

6. Optical Emission Properties

The limited implantation depth (typically 100–200 nm) and fluence do not produce a sufficient number of nanocrystals to

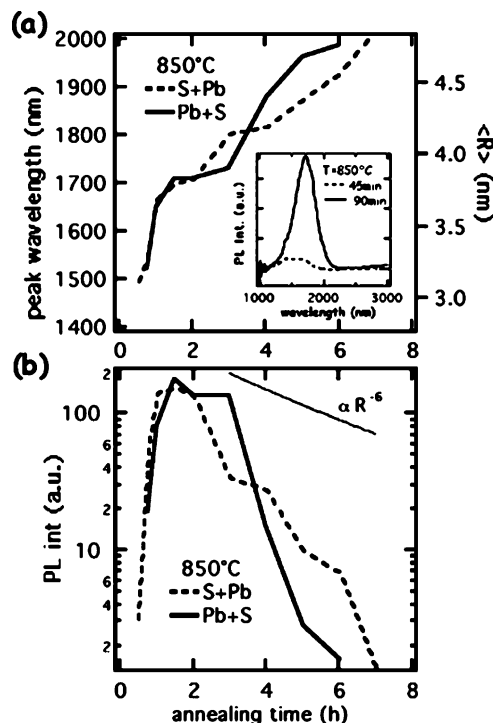


Figure 12. PL emission properties of S + Pb and Pb + S sequentially implanted sample as a function of annealing time at 850 °C/1 h. Increase of the peak wavelength maximum, the inset being examples of PL spectra (a). On the right side of the graph is the mean radius, corresponding to the peak wavelength, estimated by the model in ref 19. PL intensity variations (b). The thin line is proportional to R^{-6} as estimated with the help of data in (a).

observe optical absorption in our samples, but a rather intense PL due to the first exciton state was observed¹² in the (S + Pb) implanted samples, and more results of this system are discussed below. On the other hand, the (Se + Pb) sequentially implanted samples failed to display any PL despite TEM evidence for the presence of PbSe nanocrystals with a radius below 7 nm after annealing (Figures 6b and 8b). Assuming, for simplicity, a gap $E_g = 0.28$ eV, as deduced from the nanocrystal size-gap relation,¹⁹ and an effective mass $m^* = 0.077 m_e$, such nanocrystals should have emitted light at wavelengths below about 3 μm (which was the spectral detection limit of our PbS detector). The absence of any signal was possibly due to PL quenching by very efficient photoexcited carriers or to surface defect-induced nonradiative transitions. Why this should affect PbSe and not PbS remains unclear.

The (S + Pb) samples exhibited significant PL as soon as nanocrystal growth set in. Figure 12a shows the PL of a sequentially implanted sample annealed at 850 °C for different durations. The PL signal was centered at about 1.5 μm (fwhm = 0.5 μm) after a 30 min anneal. As the annealing time increased, the PL line intensity increased considerably and displayed a red-shift (centered at 1.6–2.0 μm after a 2–3 h anneal) due to nanocrystal growth. Further annealing led to a decrease in the PL intensity, which disappeared after an 8 h anneal (Figure 12b). The nanocrystal radius, deduced from the PL intensity maximum via ref 19 (right-hand side of Figure 12a), may be compared to the values measured via TEM after several anneals. For example, after a 1 h anneal at 850 °C, we find $\langle R \rangle = 3.8$ nm from TEM, corresponding to a lowest exciton state emission wavelength at 1.6 μm , according to the model. Other experimental TEM determinations of mean nanocrystal radii for longer anneals ($\langle R \rangle$ (900 °C/1 h) = 4.1 nm, $\langle R \rangle$ (900 °C/2 h) = 4.5 nm, and $\langle R \rangle$ (900 °C/4 h) = 5.1 nm) also compare

favorably with values deduced from PL experiments in Figure 12a. We note that such estimates are only indicative, the model in ref 19 being valid for perfectly spherical nanocrystals with infinite confinement barriers, whereas our microstructures include polycrystalline nanocrystals and PbSO₄/PbS interfaces. Also, and importantly, our comparison concerns the average nanocrystal sizes, whereas the rather broad observed PL emission line presumably involves contributions from nanocrystals of different sizes. But the correlation between the average PL peak wavelength shift and nanocrystal size is a reasonable indication that the observed PL is due to the confined exciton within the PbS nanocrystals, and the relation between PbS nanocrystal sizes, average PL emission wavelength, and PL intensity provides additional information on the growth mechanisms. For example, the PL intensity increase with annealing time was very sharp, whereas the PL position remained fairly constant. This is consistent with TEM observations (Figure 4a), showing that growing nanocrystals very rapidly reach a mean radius of about 3–3.5 nm at the expense of smaller amorphous (hence nonemitting) clusters.

Regarding the sharp PL intensity decrease after a 2 h anneal at 850 °C (Figure 12b), we note the following. The PL intensity I_{PL} scales as $n \cdot f_{\text{osc}}$ where n is the PbS nanocrystal density and f_{osc} , their oscillator strength. Predictions based on the electron and hole wave function overlap, leading to $f_{\text{osc}} \propto R^{-3}$ for a crystallite with radius R .²⁵ Assuming that the PbS nanocrystal volume fraction is conserved in our system, increasing the average nanocrystal size leads to a density decrease varying as $n \propto R^{-3}$ and, hence, to the $I_{\text{PL}} \propto R^{-6}$ dependence shown as a thin line in Figure 12b. In fact, the experimental PL intensity decreased much more rapidly. This discrepancy may be due to several causes: a PbS nanocrystal volume fraction decrease by outdiffusion from the sample during long anneals (Figure 5), a partial reverse transformation of PbS into PbSO₄, and/or the increasing influence of nonradiative paths as annealing proceeds.

7. Conclusion

We have synthesized lead chalcogenide nanocrystals by sequential implantation of the components into pure silica. The redox properties of the nanocrystal constituents, especially those of the chalcogens, are shown to have a major influence on the nanocrystal microstructures as well as on their growth characteristics, final size distribution, and spatial repartition. We have shown that the use of ion implantation as a means of synthesis cannot bypass these redox properties because the required postannealing process activates the chemical interactions of the implanted elements among themselves and with the host. As a result, it is impossible to rely on the initial implantation profiles to predict the nanocrystals' depth distribution; the coupling between diffusion and precipitation must be taken into account. The rather complex chalcogen chemistry also leads to multiple nucleation mechanisms, possible transient nanocrystal chemical compositions, and differing final nanocrystal compositions for

different chalcogens (e.g., PbS and PbSe versus pure Te). Its effect on diffusion leads to lack of growth control and affects the size distribution broadening. Controlling the redox chemistry (chemical nature of the matrix, composition of the annealing atmosphere) is a prerequisite to reaching better control over growth and, hence, over the lead chalcogenide optical properties. In the case of PbS, we have succeeded in obtaining intense, although rather broad, optical emission in the range 1.5–2.0 μm .

References and Notes

- (1) Borelli, N. F.; Smith, D. W. *J. Non-Cryst. Solids* **1994**, *180*, 25.
- (2) Lipovskii, A. A.; Kolobkova, E. V.; Petrikov, V. D. *Proc. SPIE-Int. Soc. Opt. Eng.* **1997**, *2967*, 30.
- (3) Lipovskii, A.; Kolobkova, E.; Petrikov, V.; Kang, I.; Olkhovets, A.; Krauss, T.; Thomas, M.; Silcox, J.; Wise, F.; Shen, Q.; Kycia, S. *Appl. Phys. Lett.* **1997**, *71*, 3406.
- (4) Craievich, A. F.; Alves, O. L.; Barbosa, L. C. *J. Appl. Crystallogr.* **1997**, *30*, 623.
- (5) Craievich, A. F.; Kellermann, G.; Barbosa, L. C.; Alves, O. L. *Phys. Rev. Lett.* **2002**, *89*, 235503.
- (6) Meldrum, A.; Withrow, S. P.; Zuhr, R. A.; White, C. W.; Boatner, L. A.; Budai, J. D.; Anderson, I. M.; Henderson, D. O.; Wu, M.; Ueda, A.; Mu, R. *Microcryst. Nanocryst. Semicond. 1998, Symp.* **1998**, *536*, 317.
- (7) Meldrum, A.; Sonder, E.; Zuhr, R. A.; Anderson, I. M.; Budai, J. D.; White, C. W.; Boatner, L. A.; Henderson, D. O. *J. Mater. Res.* **1999**, *14*, 4489.
- (8) White, C. W.; Budai, J. D.; Meldrum, A. L.; Withrow, S. P.; Zuhr, R. A.; Sonder, E.; Purezky, A.; Geohegan, D. B.; Zhu, J. G.; Henderson, D. O. *Atomistic Mechanisms in Beam Synthesis and Irradiation of Materials*; Materials Research Society: Warrendale, PA, 1999; p 399.
- (9) Meldrum, A.; White, C. W.; Boatner, L. A.; Anderson, I. M.; Zuhr, R. A.; Sonder, E.; Budai, J. D.; Henderson, D. O. *Nucl. Instrum. Methods Phys. Res., Sect. B* **1999**, *148*, 957.
- (10) Espiau de Lamaestre, R. Ph.D. Thesis, University Paris XI, 2005; Espiau de Lamaestre, R.; Bernas, H. To be published.
- (11) Espiau de Lamaestre, R.; Jomard, F.; Majimel, J.; Bernas, H. *J. Non-Cryst. Solids*, **2005**, *351*, 3031.
- (12) Espiau de Lamaestre, R.; Bernas, H.; Ricolleau, Ch.; Majimel, J. IBMM2004, *Nucl. Instrum. Methods Phys. Res. Sect. B*, submitted for publication.
- (13) Volf, M. B. *Chemical Approach to Glass*; Elsevier Science Publishing Company Inc.: New York, 1984; S: p 524; Se: p 544; Te: p 554.
- (14) Shelby, J. E. *Handbook of Gas Diffusion in Solids and Melts*; ASM International: Materials Park, OH, 1996; p 191.
- (15) Espiau de Lamaestre, R.; Bernas, H.; Jomard, F. *Nucl. Instrum. Methods Phys. Res., Sect. B* **2004**, *216*, 402.
- (16) Chaumont, J.; Lalu, F.; Salome, M.; Lamoise, A. M.; Bernas, H. *Nucl. Instrum. Methods Phys. Res.* **1981**, *189*, 193.
- (17) Ziegler, J. F.; Biersack, J. P.; Littmark, U. *The Stopping and Range of Ions in Solids*; Pergamon Press: New York, 1985.
- (18) Bernas, H.; Chaumont, J.; Cottureau, E.; Meunier, R.; Traverse, A.; Clerc, C.; Kaitasov, O.; Lalu, F.; Ledu, D.; Moroy, G.; Salomé, M. *Nucl. Instrum. Methods Phys. Res., Sect. B* **1992**, *62*, 416.
- (19) Wang, Y.; Herron, N. *J. Chem. Phys.* **1991**, *95*, 525.
- (20) Trinkaus, H.; Mantl, S. *Nucl. Instrum. Methods Phys. Res., Sect. B* **1993**, *80/81*, 862.
- (21) Porter, D. A.; Easterling, K. *Phase Transformations in Metals and Alloys*; Chapman and Hall: London, 1992.
- (22) Haasen, P. *Physical Metallurgy*; Cambridge University Press: New York, 1996.
- (23) Kuehmann, C. J.; Voorhees, P. W. *Metall. Mater. Trans. A* **1996**, *27*, 937.
- (24) Limpert, E.; Stahel, W. A.; Abbt, M. *Biosci.* **2001**, *51*, 341–352.
- (25) Kayanuma, Y. *Phys. Rev. B* **1988**, *38*, 9797.